

## DETECTING INTRACLUSTER GAS MOTION IN GALAXY CLUSTERS: MOCK ASTRO-E2 OBSERVATIONS

Andrew Pawl<sup>1</sup>, August E. Evrard<sup>1,2,3</sup>, and Renato A. Dupke<sup>1,2</sup>  
apawl@umich.edu, evrard@umich.edu, rdupke@umich.edu

Draft version April 23, 2019

## ABSTRACT

We explore the detectability of bulk motions in the X-ray emitting intracluster medium (ICM) using a catalog of 1,836 mock Astro-E2 observations of simulated clusters of galaxies. We generate high resolution mock spectra for two observing strategies: a four-pointing mosaic and a single centralpointing. Normalizing to 200 (400) photons in the iron K region for the mosaic (central) study, we fit Poisson realizations of each simulated spectrum to a velocity broadened isothermal plasma emission model. We confirm that the velocity characteristics (mean and dispersion) returned by the spectral fittings are unbiased measures of the emission-weighted values within the observed region, with scatter  $55 \text{ km s}^{-1}$ . The maximum velocity difference between mosaic element pairs  $v_{\max}$  has a 6% likelihood of being transonic ( $v_{\max} = 0.5c_s$ ), and the likelihood falls steeply,  $p(v_{\max} = c_s) \approx 4\%$ , at high Mach number. The velocity broadening parameter  $v$  from the centralpointing fit exceeds the thermal value in 49% of the cases, with again a  $v^{-4}$  tail at large dispersion. We present as case studies the clusters that yield the strongest signal for each observing strategy.

Subject headings: clusters: general | clusters: ICM | cosmology: observations | intergalactic medium | X-rays: clusters

## 1. introduction

In a hierarchical model of structure formation, galaxy clusters are built from the continuous accretion of subsystems and, therefore, clusters are expected to frequently display visible signatures of mergers. Binary clusters (Jones & Forman 1984) offer evidence of precursor systems while clusters with multiple emissivity peaks, strong isophotal twists and ellipticity variations possess morphologies associated with the later stages of merger evolution (Mohr, Fabricant & Geller 1993; Buote & Tsai 1996). Bulk motions and turbulence of the hot intracluster medium (ICM) are thus expected to be evident in line emission from the plasma, in particular from helium-like iron, FeXXV (Dupke & Bregman 2001a,b; Sunyaev et al. 2003; Inogamov & Sunyaev 2003).

X-ray satellite missions to date have had spectrometers with energy resolutions marginally adequate for the observation of cluster velocity structure (Dupke & Bregman 2001a,b). The new microcalorimeter technology employed in the X-ray Spectrometer (XRS) instrument aboard the Astro-E2 satellite, however, is designed to have an energy resolution of 6.5 eV FWHM across its entire frequency range (Furusho et al. 2004), giving a response contribution to the line broadening of 1.5 eV and finding line centroids to within about 2 eV. This implies that the instrument will be sensitive to velocity structure down to

100 km/s near the Fe K line. Since the infall velocity of material accreting onto a large cluster can be an order of magnitude larger than this limit, Astro-E2 will enable unambiguous observation of gas motion in dynamically active systems.

Cosmological simulations provide a framework for investigating the statistical properties of the internal gas velocity

distribution. In addition, access to the complete 3-D structure and time evolution of the simulated clusters can, through comparative studies of observations and simulations, help unfold the evolutionary history and dynamical state of observed clusters.

Until now, no estimate of the frequency with which clusters should show detectable velocity structure has been made. In this paper, we evaluate the fraction of clusters expected to show observable structure in the Fe K line by performing mock Astro-E2 observations of a catalog of simulated clusters. The simulations model clusters in a CDM cosmology with a preheated assumption for the ICM that matches observed local scaling laws (Bialek, Evrard & Mohr 2001).

In x2, we describe the simulation sample and the strategies we use to produce mock observations. Results in the form of statistical expectations and illustrative examples are presented in x3. We summarize our findings in x4.

## 2. mock observations

## 2.1. Preheated Cluster Simulations

We use a catalog of 68 preheated clusters evolved with P3M SPH (Evrard 1988) under a preheated assumption for the ICM. The level of entropy introduced into the initial conditions is tuned to 105.9 keV cm<sup>-3</sup> in order to match the observed scalings of luminosity and ICM mass with temperature (Bialek et al. 2001).

The simulations were produced using a multi-step procedure outlined in (Bialek et al. 2001). The underlying cosmology is flat, concordance model with  $\Omega_m = 0.3$ ,

$\Omega_b = 0.03$ ,  $\Omega_\Lambda = 1.0$ , and  $h = 0.7$ , where the Hubble constant is defined as  $100h \text{ km s}^{-1} \text{ Mpc}^{-1}$  and  $\Omega_\Lambda$  is the power spectrum normalization on 8h<sup>-1</sup> Mpc scales.

<sup>1</sup> Michigan Center for Theoretical Physics, University of Michigan, Ann Arbor, MI<sup>2</sup> Department of Astronomy, University of Michigan, Ann Arbor, MI<sup>3</sup> Department of Physics, University of Michigan, Ann Arbor, MI

Details of the full ensemble will be presented in Bialek, Evrard & Mohr (2005). One member of the ensemble contained a prominent cold front feature, generated during a merger by the separation and resultant adiabatic cooling of the core of an infalling satellite, as discussed by Bialek et al. (2002).

The cosmological values assumed for the models are in line with WMAP allowed parameters, with the exception of the baryon fraction. The value  $b_{\text{m}} = 0.1$  used in the simulations is lower than WMAP value 0.16–0.1 (Bennett et al. 2003). The mass fraction in intracluster gas is expected to be less than the cosmic baryon fraction due to galaxy formation and energy exchange with dark matter during mergers (Thomasson & Couchman 1992). The former process removes 15–20% of the baryons from the hot phase in rich clusters while the latter expels 10% of the gas from the potential (Frenk et al. 1999). Still, the model gas fractions are likely to be somewhat low compared to current observational estimates. However, in the results presented here, the baryon fraction affects only the normalization of the ICM X-ray spectrum. Our mock spectra are tuned to a fixed line normalization, which at fixed cluster mass scales  $\propto (b_{\text{m}})^2 t_{\text{exp}}$ , with  $t_{\text{exp}}$  the exposure time. A higher or lower baryon fraction can thus be absorbed by appropriate rescaling of the exposure.

The configuration of each simulation is stored at twenty output times, spaced equally in time from the initial redshift  $z_i = 20.82$  to the present. We employ the final nine outputs of the 68 models in this study. This yields 612 cluster realizations which we treat, under an ergodic hypothesis, as statistically independent. The time separation of 0.7 Gyr between outputs typically exceeds the crossing time at  $r_{200}$ , justifying the ergodic assumption.

We further enhance our sample by considering the line of sight (LOS) velocity structure of each realization along three perpendicular axes. Although these projections are linked by dynamics, the LOS velocity structure is genuinely independent. We thus have three projections of each of the 612 realizations, for a total of 1,836 exposures. The members of the simulated sample range in spectral temperature from 1.5 keV to about 8 keV, with cluster masses  $M_{200}$  ranging from  $0.015\text{--}2.4 \times 10^{15} M_{\odot}$ .

The derived spectra and images, along with associated parameters describing the simulations are publicly available as part of VCE, the Virtual Cluster Explorer<sup>4</sup>.

## 2.2. Creating the Mock Exposures

We create mock Astro-E 2 spectra of these realizations following two observing programs illustrated in Figure 1. The first program involves a search for velocity gradients by measuring differences in the mean velocity of the Fe K lines for multiple pointings of the Astro-E 2 instrument. This strategy allows one to measure both the magnitude and a crude direction of the velocity gradient. Multiple pointings are required because the average angular resolution of the X-ray telescopes on Astro-E 2 is  $1.9^{\circ}$  and the detector configuration is roughly a square with  $2.9^{\circ}$  on the side. Since less than 60% of the encircled energy is contained within  $2^{\circ}$ , spatially resolved spectroscopy using sub-

regions of the detector will be highly contaminated with photons from neighboring regions. Therefore, to carry out this observational strategy, we create four mock spectra of each cluster projection in a  $2 \times 2$  box centered on the cluster. The second program involves searching for extrathermal broadening of the Fe K line using a single, central pointing.

see file figure1.jpg

Fig. 1. | Observing strategies overlaid on the surface brightness map for a typical cluster in our catalog. The black boxes indicate the fields for the four-pointing mosaic program while the white box shows the central field of the line broadening program. Each field is 2.9 arcmin on a side, the FOV of Astro-E 2, which corresponds to 321 kpc at  $z = 0.1$ .

The thermal plasma emission spectra for this study are compiled using the APEC code (Smith et al. 2001) from the XSPEC 11.3.1 suite of spectral analysis tools (Maud 1996). APEC allows us to include thermal broadening of the line spectra by setting the APEC THERMAL toggle to 'yes'. Further, XSPEC allows us to fold in the anticipated XRS response functions<sup>5</sup>. We use XSPEC/APEC to write a reference table of spectra in flux units at 176 temperatures spaced logarithmically to cover our range of interest. This spectral table is limited to an energy range appropriate for studying the Fe K complex. The flux spectra are limited to the interval 5.9 keV to 6.4 keV. All spectra are generated with the cluster at a fiducial redshift of 0.1, so that the Fe XXV K line is centered at 6.09 keV and the Fe XXVI K line at 6.33 keV (the hydrogen-like iron line is actually two separate lines with centers at 6.32 and 6.34 keV as a result of fine structure (Verner, Verner & Ferland 1996)). Figure 2 shows the K line region of reference spectra at a few relevant temperatures.

To create a simulated spectrum for a mock observation, we interpolate on the reference flux table to generate an emission spectrum for each gas particle of the simulation contained in the Astro-E 2 FOV. There are typically 1000 particles in the the FOV, and their contributions

<sup>4</sup> <http://vce.physics.lsa.umich.edu>

<sup>5</sup> obtained at <http://heasarc.gsfc.nasa.gov/docs/astroe-prop-tools/xrsrmat.htm>

are summed to obtain the complete spectrum. To convert the resulting flux spectrum into an XRS count spectrum, we first define an exposure time that requires either 200 or 400 total counts in the Fe K line region within the energy range of interest, i.e., 6.0–6.2 keV. (The 200 count criterion applies to the four-pointing mosaic study, while 400 counts are used for the central pointing spectra.) A single, discrete Poisson realization of each spectrum is then created, using the `poidev` routine of Press et al. (1992).

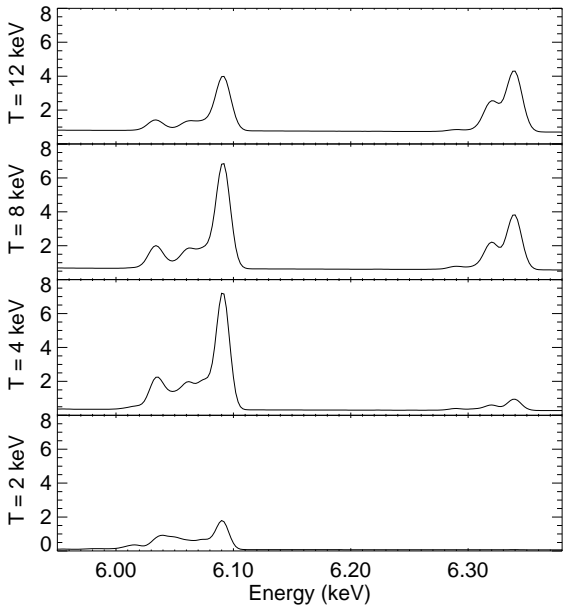


Fig. 2. | APEC thermal spectra of 0.4 solar metallicity plasma (arbitrary flux units) in a narrow energy range centered on the iron K complex at redshift  $z = 0.1$  are shown for typical temperatures of plasma in the simulations. The Astro-E 2 XRS energy response has been folded in.

### 2.3. Additional Assumptions

The iron abundance of the ICM is not determined by cluster simulations, and so has to be assumed based on data from observed clusters. Given the small field of view of the XRS on-board Astro-E 2, we are probing regions fairly close to the cluster's core ( $< 0.2 r_{200}$ ). The iron abundance in cluster cores is typically higher than the average over the whole cluster, due to the frequent presence of central metal abundance gradients in cold core ("cooling flow") clusters (Ulmer et al. 1987; White et al. 1994), which constitute the majority of clusters. Assuming an average central iron abundance of 0.27 solar for non-cold core clusters and 0.47 for cold core systems (D'Elia et al. 2004), and recognizing that 70–90% of an X-ray limited sample of clusters have cold cores (Edge, Stewart & Fabian 1992), we obtain an average central iron abundance of 0.4 relative to the solar photospheric values of Anders & Grevesse (1989). This is the value assumed throughout this work.

One of the main obstacles in measuring velocities of the intracluster gas with current spectrometers is the inability to accurately calibrate the temporal and spatial fluctuations of instrumental gain, the conversion of pulse-height into photon energy (Dupke & Brégnier 2001b). For the case of CCDs the intrachip (positional-dependent) gain changes are related to the charge transfer inefficiency,

which evolves with time. Often these fluctuations are on the same order as the velocities one is trying to measure. Although this is not an issue for the XRS calibrator, small drifts in the temperature of the detector heat sink can cause global gain variations. The absolute precision of the gain variations in the XRS is expected to be  $1\text{--}2\text{ eV}$  ( $50\text{--}100\text{ km s}^{-1}$ ) at 6 keV and will have to be inserted into the uncertainties of the velocity measurements described here (Figueroa, personal communication, 2004). These uncertainties were not incorporated in our evaluations of velocity gradients, but they do not affect the overall results derived in this work. Similarly, for the purpose of this paper we do not take a background spectrum. The main source of background for the XRS is due to energy deposition in the detector by energetic protons. However, given the small detector size and the distribution of the proton energy spectrum, its contribution in the frequencies of interest ( $< 10\text{ keV}$ ) are expected to be negligible ( $< 2\text{--}5\%$ ) for our mock observations.

Finally, in this paper we assume that the intracluster plasma is optically thin. Gil'fanov, Sunyaev & Churazov (1987) have pointed out that this may not always be true for the Fe K line. Resonant scattering (the absorption and immediate re-emission of a Fe K line photon by an Fe ion) can be significant in the cores of clusters. If so, the line emission from the cluster core is reduced because of the scattering of photons out of the field of view. Early evidence for resonant scattering (Molendi et al. 1998) seen in the Perseus cluster has proven ambiguous, allowing other possible interpretations such as an overabundance of Ni due to the central SN Ia ejecta dominance (Dupke & Arnaud 2001). XMM observations of the Perseus cluster have confirmed the Ni overabundance scenario (Gastaldello & Molendi 2004). The absence of observed scattering has since been used as evidence for the presence of turbulent (non-thermal) velocities in clusters' cores (Churazov et al. 2004).

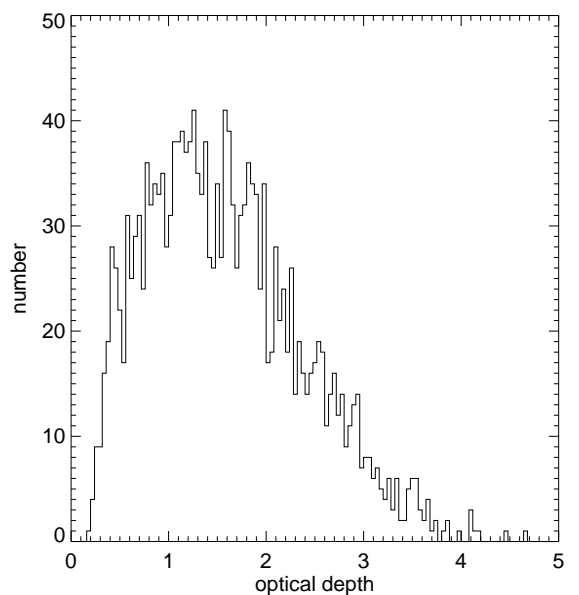


Fig. 3. | Histogram of the optical depth for the central pointing of the 1836 cluster projections used in this study.

We have computed the optical depth for the central pointing of each cluster projection used in this study (see Appendix A for details) in Figure 3. To be conservative, we calculate the optical depth through the entire cluster. The results are shown in Figure 3. When the non-thermal velocities seen in the emission line are included, the average optical depth for the Fe X XV K line in the FOV of the central pointing is 1.58, with standard deviation 0.8. The results of Churazov et al. (2004) and Gilfanov et al. (1987) show that for  $\tau = 1.6$ , the flux and the line width near the cluster core will show approximately a 30% reduction. Additionally, it is possible that some deformation of the line profile may occur (Gilfanov et al. 1987). None of these effects would introduce errors in the line centroids we recover. The reduction in line width would affect our line broadening study, but, as our results will show, a 30% reduction is not prohibitive.

#### 2.4. Velocity Gradients Via Multiple Pointings

We first investigate the LOS velocity structure of the simulated clusters by creating one set of four mock exposures tiled around the most bound position of the relevant cluster, as shown by boxes 1-4 in Figure 1. The mock exposures result in four separate Poisson-noise-added spectra. We rebin these spectra to ensure at least 15 counts in each bin using the `grppha` routine from the `FTOOLS` package<sup>6</sup>.

We fit the grouped spectra to find the position of the centroid velocity  $v_i$  of the Fe K line in image  $i$ . The spectra are fit in XSPEC to a BAPEC model. BAPEC is a thermally broadened PEC that allows for additional Gaussian velocity broadening under a parameter  $v$ .

The resulting centroid positions are divided into velocity gradients  $v_{ij} = v_i - v_j$  among the six distinct pairs of the four pointings. Thus, from our 1,836 independent cluster projections we generate 7,344 spectra which are used to give 11,016 velocity differences.

An advantage of working with simulated clusters is our complete knowledge of the underlying velocity structure of the gas. In an isothermal cluster, the redshift of the line center could be recovered from the density-squared weighted velocity (henceforth called the EM-weighted velocity) of the emitting gas. Our simulated clusters are not isothermal, but it happens that the Fe K line flux is not strongly temperature dependent within the temperature range expected for hot ICM gas. The peak flux varies by only a factor of 2 over a temperature range from 3 keV to 12 keV. For this reason, an EM-weighted velocity can be regarded as a predictor of the line center that would be recovered from a spectral analysis. Therefore, as a point of comparison we also generate the EM-weighted radial velocity of each Astro-E 2 FOV directly from the simulation.

To minimize systematic issues, we find the velocity of each FOV for a given cluster projection relative to the mean value of the four FOV's for that projection. We repeat this procedure using the BAPEC redshift values. A histogram of the differences between the velocities recovered in this way from the BAPEC spectral fits and from the EM-weighted averages is shown in Figure 4. Note that the XRS instrument is expected to find line centroids with a fitting resolution of about 2 eV near the Fe K com-

plex<sup>7</sup>, which corresponds to an expected fitting accuracy of 100 km/s near the Fe K line. The histogram of differences has a dispersion of 54 km/s<sup>1</sup>. We conclude, therefore, that 200 counts in the line (with grouping applied) results in velocity measurement accuracies very comparable to the expected 2 eV pre-launch instrument response.

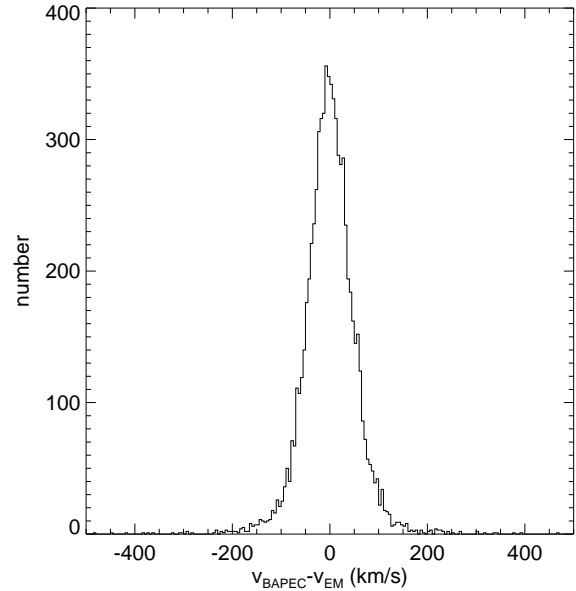


Fig. 4. Histogram of the differences between velocities recovered from BAPEC fittings and those generated using EM-weighted velocities.

#### 2.5. Nonthermal Velocities Via Line Broadening

Line broadening is another means of recovering the velocity structure of the emitting plasma. As described by Sunyaev et al. (2003) and by Inogamov & Sunyaev (2003), the large atomic mass of iron suppresses thermal line broadening, making the Fe K line width a sensitive probe of bulk gas motion. For line broadening studies, only one mock Astro-E 2 image of each cluster centered on the most bound position is used, giving a total of 1,836 observations. For this study, our final spectra are generated by requiring 400 counts in the line region (6.0-6.2 keV). The velocity broadenings of the spectra are returned as the parameter  $v$  of the BAPEC fit.

Once again, we perform a theoretical check on these results. The EM-weighted velocity dispersion of the particles within the Astro-E 2 field of view is taken to be a predictor of the best-fit BAPEC  $v$  parameter. The differences between these two measures of velocity broadening are shown in Figure 5. The dispersion for the entire data set of 1,836 broadenings is 55 km/s<sup>1</sup>.

The data of Figure 5 show evidence of a systematic effect. The mean value of  $v$  (BAPEC)  $- v$  (EM) is clearly offset from zero. For the complete sample, it is 26.6 km/s<sup>1</sup>. This systematic is at least partly explained by the fitting process. The spectral resolution (FWHM) of the XRS is about 6.5 eV near the Fe K line, corresponding to a response contribution to the broadening of  $r = 1.5$  eV or  $75$  km/s<sup>1</sup>. This implies that XSPEC should

<sup>6</sup> see <http://heasarc.gsfc.nasa.gov/docs/software/ftools.html>

<sup>7</sup> see [http://legacy.gsfc.nasa.gov/astroe2/nra\\_info/astroe2\\_td.pdf](http://legacy.gsfc.nasa.gov/astroe2/nra_info/astroe2_td.pdf)

be unable to recognize physical broadenings significantly less than  $75 \text{ km s}^{-1}$ . Clusters with EM-weighted broadenings significantly less than  $75 \text{ km s}^{-1}$  are therefore reported as zero broadening in the BAPEC fit. Removing projections with zero reported broadening shifts the mean value of  $\sigma_v(\text{BAPEC}) - \sigma_v(\text{EM})$  to  $13.4 \text{ km s}^{-1}$  and leaves the dispersion unchanged.

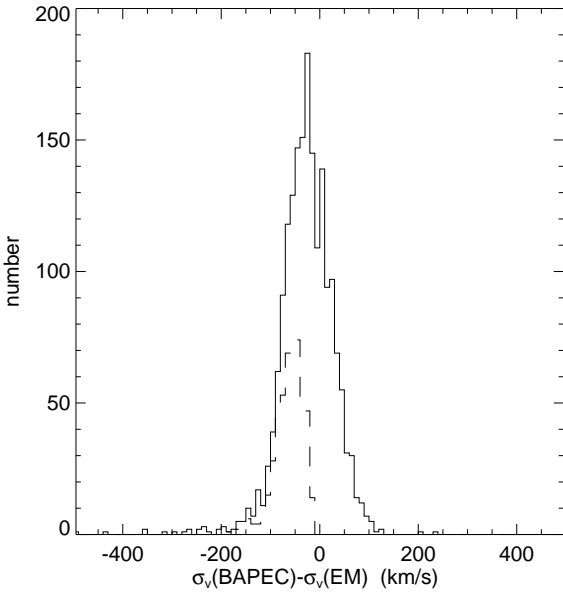


Fig. 5. Histogram of the differences between the velocity broadening parameter returned by BAPEC and the EM-weighted velocity dispersion. The dashed line denotes the portion of the sample with BAPEC uncertainties  $> 5\%$  (the "zero broadening" sample).

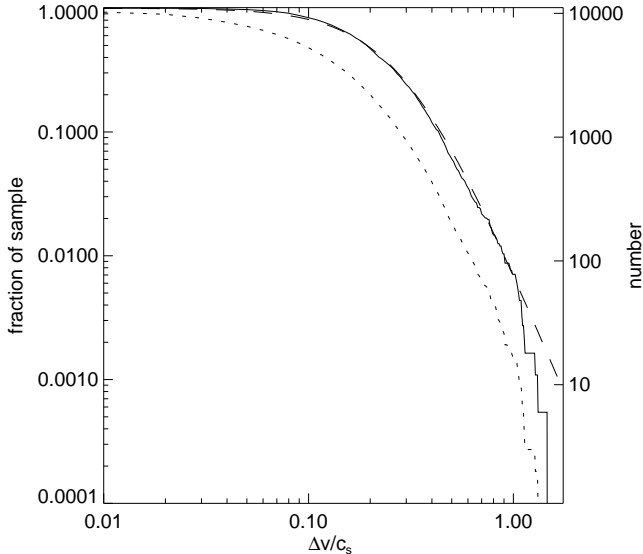


Fig. 6. Cumulative likelihoods of the normalized velocity gradients  $v=c_s$  are shown for the case of only maximum velocity differences (solid) and the case of all pointing pairs (dotted). A fit to the former is given by equation (3) (dashed).

### 3. results

#### 3.1. Velocity Gradients

Figure 6 shows the cumulative frequency distribution of velocity differences, normalized to the sound speed in the ICM, that result from the four-point tiling program.

Because the ICM temperature is determined by the gravitational potential of a cluster, the sound speed in the ICM gas is approximately

$$c_s = \frac{s}{\sqrt{\frac{5kT_{\text{ICM}}}{3m_p}}} \propto \frac{p}{m_p} \quad (1)$$

where  $m_p$  is the average mass per ICM particle. Since the bulk velocity structure of the ICM is determined by mergers also driven by the gravitational potential of the dominant cluster, one expects infall velocities

$$v_{\text{inf}} \propto \frac{p}{2} \quad (2)$$

All explicit dependence on  $p$ , hence on the size of the cluster, vanishes when infall velocity is scaled by the sound speed. For each simulation, we determine the sound speed from the best-fit spectral temperature of an isotherm at the  $0.5 - 9.5 \text{ keV}$  emission of plasma within  $r_{500}$ , the radius within which the mean interior density is 500 times the critical value.

The solid line in Figure 6 shows the cumulative frequency distribution of the maximum velocity gradient among the six pairs of each 4-point mosaic. The fraction of cluster projections in the sample of 1,836 with a maximum normalized velocity difference larger than some value  $x$  is well fit by

$$f(v_{\text{max}} = c_s > x) = 1 + \frac{x}{0.30}^{-2} \quad (3)$$

The number of cluster projections in our sample with a maximum normalized velocity difference larger than half the sound speed for the cluster is 111, or approximately 6.0% of the sample. The total number of splittings out of the 11,016 measured to be larger than  $0.5c_s$  is 200, or approximately 1.8%.

The likelihood of high Mach number splittings falls dramatically, as  $(v=c_s)^{-4}$ . The lack of very high Mach collisions is expected from the arguments given in equations (1) and (2) above. One anticipates  $v_{\text{inf}} < a \text{ few } c_s$  because larger Mach numbers could not be generated by hierarchical clustering driven by gravity. Our mock spectral measurements are consistent with this expectation. Note that the quoted value of the sound speed always refers to the dominant member of a merging pair. With respect to  $c_s$  of the smaller member, high Mach number collisions are certainly possible. But the measured "broad-beam" temperature, and sound speed, of the merging system will always be driven by the larger member, and thus the data presented in Figure 6 are appropriate for comparison with observation.

For purposes of illustration, we highlight the cluster which exhibits the maximum velocity gradient: cluster number 2 at output 16 in  $y$ -axis projection. This projection yields a maximum normalized velocity gradient of  $1.47 c_s$ . Data relevant to that cluster are compiled in Figures 7-11. Figure 7 shows Poisson realizations of the four-point mosaic spectra. These spectra show that the top two quadrants of our observing pattern are blueshifted relative to the bottom two. This accurately represents the underlying motion of the cluster, as can be seen from Figure 8 which shows the perfect flux spectra generated from the simulation overlaid with the BAPEC fits to the spectra of Figure 7.

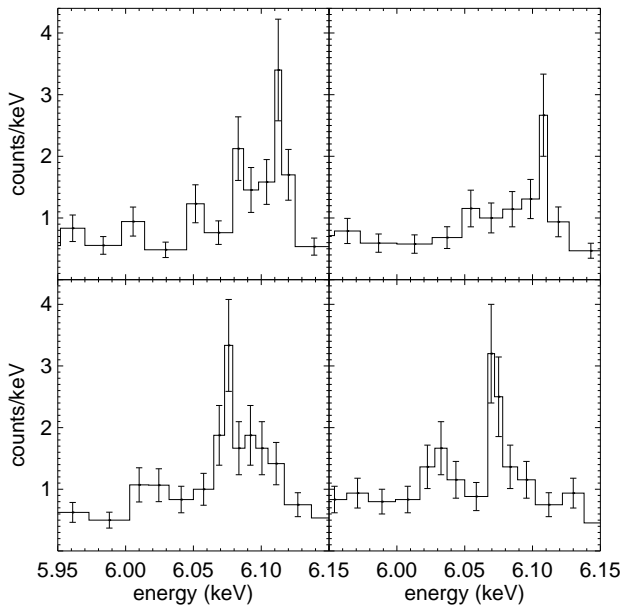


Fig. 7.1 The integrated and grouped Poisson-noised spectra used in the velocity gradient study for cluster 2 output 16, viewed along the y-axis. Each panel displays the spectrum of the corresponding four-point mosaic tile pattern shown in Figure 10.

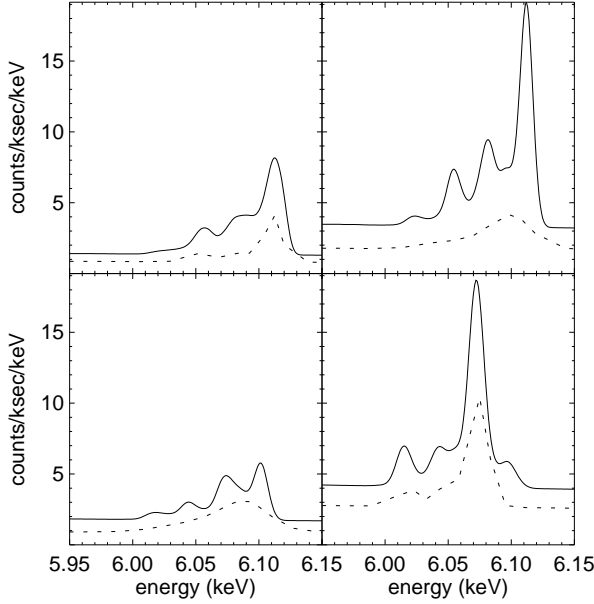


Fig. 8.1 The flux spectra generated using the APEC thermal plasma code (solid) for cluster 2 output 16 are shown along with the BAPEC tests to the Poisson spectra of Figure 7 (dashed).

The advantage of using simulations is that we can examine the underlying cause of this observed velocity structure. The lower row of images in Figures 10 and 11 shows the z-axis (orthogonal view) surface brightness and temperature maps of outputs 15, 16 and 17 of cluster 2. With this additional information, we can see that cluster 2 is extremely active. In this case it appears that the redshifted quadrants (the lower half of the mosaic) represent the primary cluster itself, which has a peculiar velocity away from the observer. The blueshifted quadrants appear to contain

a merging subcluster which is moving through the core in the negative y-direction. This subcluster can be traced in the z-axis projections starting in the upper left corner and moving toward the lower right over the course of the outputs presented in Figure 10.

see file figure9.jpg

Fig. 9.1 The line-of-sight velocity map for cluster 2, output 16 projected along the y-axis is shown along with the mock Astro-E2 fields of view. The scale key is in  $\text{km s}^{-1}$ , with positive velocities away from the observer.

### 3.2. Line Broadening

To evaluate the significance of the observed line broadenings, we normalize  $v$  recovered from BAPEC by the expected thermal velocity dispersion ( $v_{th} = \sqrt{kT/m_{Fe}}$ ). The resulting velocity dispersion distribution is presented in Figure 12. The distribution ignores 27% of the fits that return zero for the velocity broadening parameter (see x2.5). The distribution of non-zero values is fit reasonably well by

$$f(v = v_{th} > x) = 0.73 \cdot 1 + \frac{x}{1.5}^3 \quad : \quad (4)$$

Out of the whole sample, 902 cluster projections, or 49%, yield a BAPEC velocity dispersion larger than the thermal broadening of the cluster. As in the gradient case, the probability drops as  $(v = v_{th})^4$ .

Once again, we select one cluster projection to highlight as a case study. We select the cluster which exhibited the most significant line broadening: cluster 47 at output 16 viewed along the x-axis. The data relevant to this cluster is compiled in Figures 13, 14, 15 and 16. Again it is apparent that the cluster is undergoing a strong merger at this epoch. In this case, however, the merging cluster is almost directly behind cluster 47 (rather than slightly off-center as in the case of cluster 2 output 16 shown above). This on-axis configuration means that all Astro-E2 spectra in the mosaic study contain emission from the merging cluster, resulting in two-component spectra. For this reason, each image in the mosaic study will show approximately the same EM-weighted velocity, and differing mosaics yield small velocity gradients. In fact, while this projection gives a velocity dispersion more than thirteen times the thermal velocity broadening, its maximum velocity gradient in the four-point mosaic is  $0.63 \text{ s}^{-1}$ .

see file figure10.jpg

Fig. 10. | Maps show the log of the soft X-ray surface brightness (arbitrary units) for cluster 2 at outputs 15 (left), 16 (middle) and 17 (right), projected along the y (top) and z (bottom) axes of the simulation volume. The outputs correspond to epochs  $z = 0.290, 0.222$  and  $0.160$ , respectively. The width of the image box is scaled to  $2 r_{200}$  at each epoch. The mock Astro-E 2 fields of view are overlaid on the frame that displays a velocity gradient  $v = 1.47 c_s$ . Note that although this map places the observer along the positive y-axis, the spectra were generated with positive y-axis velocity yielding redshift and negative y-axis velocity giving blueshift.

see file figure11.jpg

Fig. 11. | Temperature maps (keV) for cluster 2 at outputs 15 (left) through 17 (right) along the x (top) and y (bottom) axes.

This illustrates the complexity of line broadening and multiple-imaging studies for detecting dynamically active clusters.

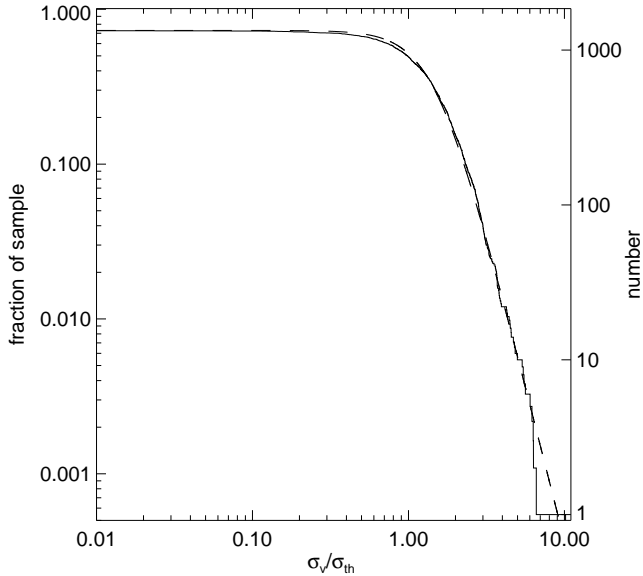


Fig. 12.| Fraction of sample with normalized velocity broadening greater than the x-axis value. The dashed line represents the given in equation (4).

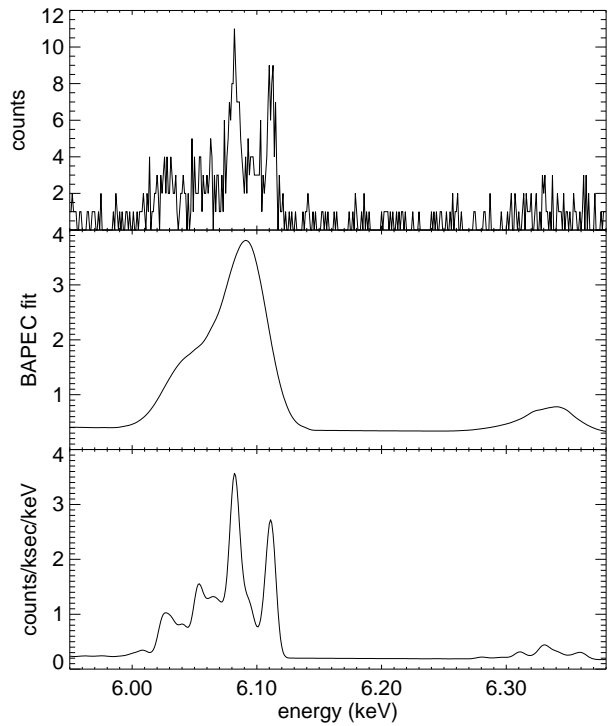


Fig. 13.| From top to bottom : the integrated spectrum , BAPEC fit, and actual flux spectrum for cluster 47, output 16 taken along the x-axis.

#### 4. conclusions

We use a large statistical sample of mock Astro-E 2 observations to investigate the expected frequency of detection of bulk motion of the ICM using the Fe XXV K line. We analyze differences in mean velocities among adjoining pointings as well as velocity broadenings in a single cen-

tral pointing of clusters developed in a CDM model and scaled to an observed redshift  $z = 0.1$ . The mean velocities and broadenings are recovered from BAPEC fits to mock Astro-E 2 spectra assuming 200 counts and 400 counts in the line region, respectively.

see file figure14.jpg

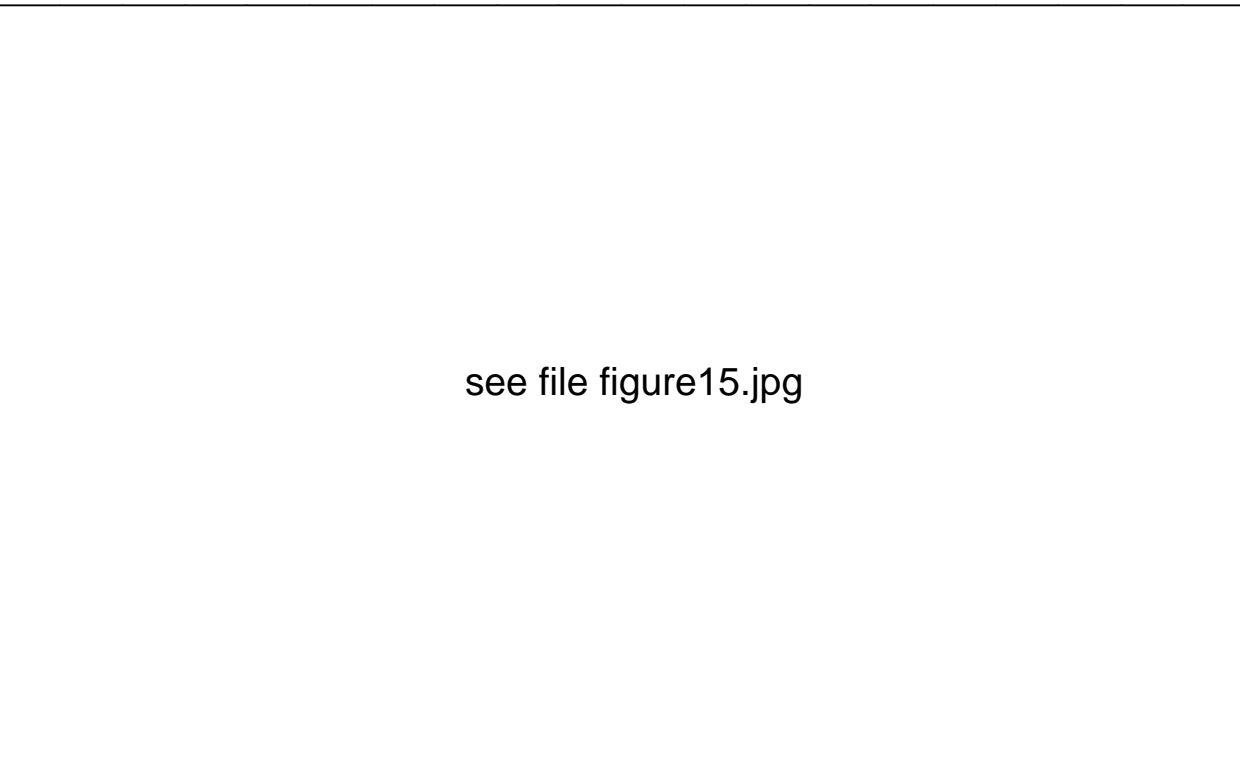
Fig. 14.| Radial velocity map for cluster 47, output 16 projected along the x-axis in the same form as Figure 9.

From the central pointings, we find that roughly one-half of randomly selected clusters display velocity broadening in the Fe K line at least as large as the thermal width, and more than 15% will be broadened at a level greater than  $2\sigma_{\text{th}}$ . In the four-point mosaic case, 6% of clusters show a maximum velocity difference that is transonic ( $v = c_s = 0.5$ ) while only 0.7% will be supersonic ( $v = c_s = 1$ ).

These fractions were obtained without any attempt to select for interesting clusters or to optimally align observations on the basis of morphology. Further, our sample is biased toward cooler (smaller) clusters. We have attempted to remove the effects of this bias by normalization, but the physical cuts represented by the  $100 \text{ km s}^{-1}$  resolution of the Astro-E 2 instrument and the significant drop in Fe K flux below 3 keV cannot be normalized away. We can only assume that an observational survey, conducted to optimize results by selecting hot clusters with bimodal galaxy velocity distributions would obtain a sample with an even larger fraction of dynamically interesting clusters.

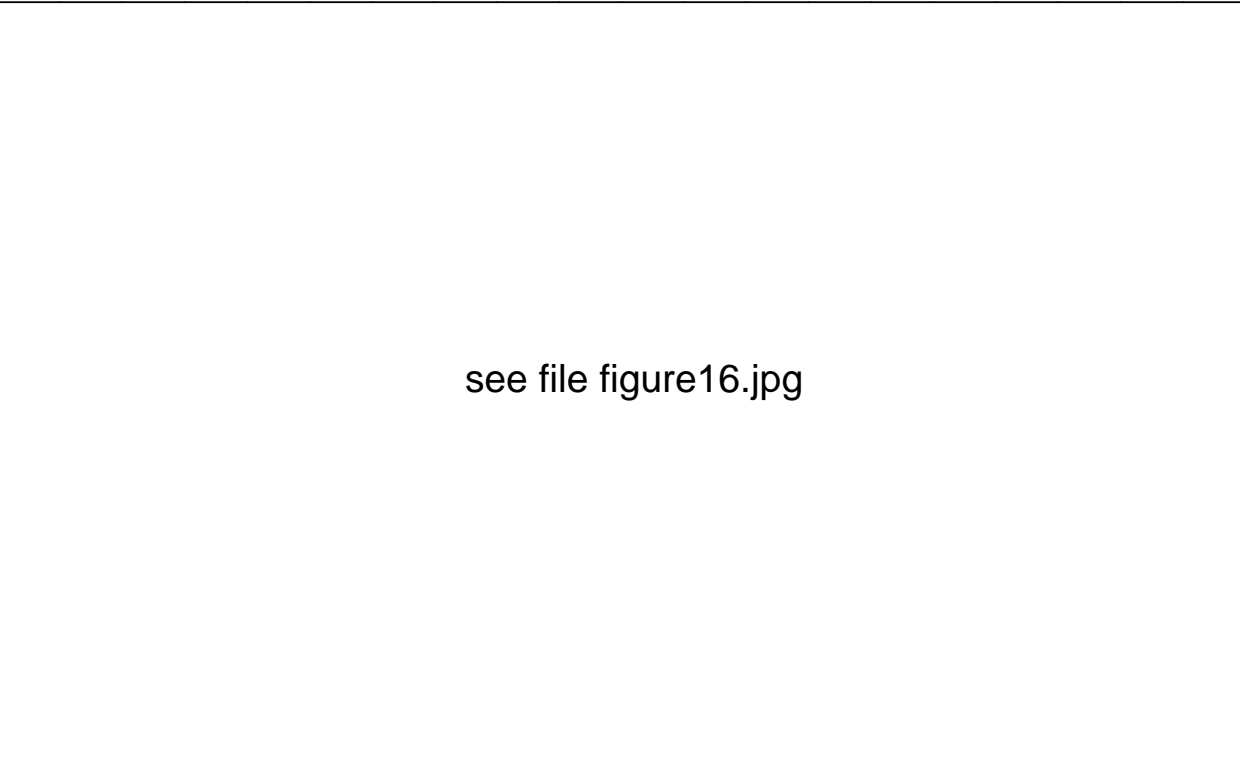
In extreme cases, however, morphological clues from X-ray observations can be misleading. We illustrate one example in which the viewing angle is nearly aligned with the infall direction of a merging satellite. Such cases possess relatively simple X-ray morphologies but show large velocity effects in the Fe K line.

This calibration exercise bears out the expectation that Astro-E 2 will be an important instrument for detecting bulk motion of ICM gas. With reasonable counting statistics, the true emission-weighted velocity within the Astro-E 2 FOV can be obtained to within  $50 \text{ km s}^{-1}$ , assuming the pre-launch gain and response estimates are accurate and that background is negligible.



see file figure15.jpg

Fig. 15.| Maps show the log of the soft X-ray surface brightness (arbitrary units) for cluster 47 at outputs 15 (left), 16 (middle) and 17 (right), projected along the x (top) and y (bottom) axes of the simulation volume. The outputs correspond to epochs  $z = 0.290, 0.222$  and  $0.160$ , respectively. The width of the image box is scaled to  $2r_{200}$  at each epoch. The mock Astro-E 2 fields of view are overlaid on the frame that displays the largest velocity broadening of the sample. Note that although this map places the observer along the positive x-axis, the spectra were generated with positive x-axis velocity yielding redshift and negative x-axis velocity giving blueshift.



see file figure16.jpg

Fig. 16.| Temperature maps (keV) for cluster 47 at outputs 15 (left) through 17 (right) along the x (top) and y (bottom) axes.

We are very grateful to K. Amaud for providing valuable input on spectral analysis tools. We also thank E. Figueroa for providing helpful information about Astro-E 2 gain. A.P. thanks J. Bialek for assistance with the manipulation of the VCE dataset and maps.

This work was supported by NASA through Chandra Theory grants TM 3-4009X and TM 4-5008X and by the NSF through ITR grant ACI-0121671. RAD also acknowledge support from NASA Grants NAG 5-3247 and Chandra GO 3-4162X.

FTS form at spectra and maps similar to those presented in this paper are available on the VCE website for selected cluster projections used in this study, including all those which exhibited splittings greater than 0.75  $c_s$  or broadenings larger than 2.5  $\sigma_{th}$ .

## APPENDIX

### computing optical depth

The optical depth for line emission obeys (Spitzer 1978):

$$(\text{d}) = \sum_j f_{jk} N_j \frac{e^2}{m_e c} \left( 1 - \frac{b_k}{b_j} e^{-h_{jk}/kT} \right) \quad (\text{A } 1)$$

where  $j$  and  $k$  label atomic states,  $h_{jk}$  is the central frequency of the line radiation emitted in a transition from  $k$  to  $j$ ,  $f_{jk}$  is the upward oscillator strength for the transition, and  $N_j$  is the column density of atoms/ions in state  $j$ . The quantities  $b_k$  and  $b_j$  measure the particle densities  $n_k$  and  $n_j$  relative to the values they would have in thermodynamic equilibrium (see Spitzer (1978) for details). At ICM densities, we expect  $b_k = 0$  for the Fe K line (Dere et al. 1997; Young et al. 2003). The oscillator strength for the K line of Fe XXV is 0.798 (Verner et al. 1996). In cgs units, then:

$$(\text{d}) = 0.0212 N_j \quad (\text{A } 2)$$

where  $N_j$  is the column density (in  $\text{cm}^{-2}$ ) of Fe XXV in the ground state.

We next simplify things by defining an average optical depth for the line:

$$\frac{p}{2} \frac{1}{\sum_k \frac{f_{jk}}{c}} (\text{d}) \quad (\text{A } 3)$$

where we define a Gaussian sigma parameterizing the width of the Fe K line. In the terminology of this paper, we use the definition:

$$\sigma = \sqrt{\frac{2}{\ln 2} \frac{\sigma_{th}^2 + \sigma_v^2}{\sigma_{th}^2 + \sigma_v^2}} \quad (\text{A } 4)$$

(note that, in keeping with the rest of this work, we have chosen a in velocity units so that the combination  $=c$  is unitless). We have computed  $\sigma_{th}$  for each cluster as a part of our line broadening study (see x3.2). We can now write (again, in cgs units):

$$\frac{4.6}{p} \frac{10^{-21} d N_j}{\sqrt{\frac{\sigma_{th}^2}{\sigma_{th}^2 + \sigma_v^2}}} : \quad (\text{A } 5)$$

The final quantity remaining to compute is  $N_j$ .

Assuming an iron abundance of 0.4 solar, we can write:

$$N_{\text{Fe}} = 2 \times 10^{-5} N_{\text{H}} : \quad (\text{A } 6)$$

Not all the iron will be in the Fe XXV ionization state, however. At maximum, 78% of the Fe will be Helium-like iron. This fraction has a non-negligible temperature dependence over the range of temperatures expected in the ICM. The peak occurs at a temperature of 3 keV. For temperatures below 1 keV or above 8 keV the fraction has fallen below 33%. For this reason, we use our knowledge of the underlying simulation to approximate the optical depth for resonant scattering in our sample of clusters. We define a function  $f(T)$  using a linear interpolation on Table 4 of Amaud & Raymond (1992). We then assign the  $i$ th gas parcel within the FOV a column density for resonant scattering given by:

$$N_{\text{FeXXV}}^i = 2 \times 10^{-5} f(T) N_{\text{H}}^i : \quad (\text{A } 7)$$

We can then sum up the column densities in the FOV to find the average optical depth in the FOV:

$$\frac{1}{\text{FOV}} = \frac{9.2 \times 10^{-26} \sum_i f(T) N_{\text{H}}^i}{\sqrt{\frac{\sigma_{th}^2}{\sigma_{th}^2 + \sigma_v^2}}} : \quad (\text{A } 8)$$

## REFERENCES

Anders, E. & Grevesse, N. 1989, *Geochim. Cosmochim. Acta*, 53, 197  
 Amaud, K.A. 1996, *Astronomical Data Analysis Software and System 5*, eds. Jacoby, G. and Barnes, J., AASP Conf. Series volume 101 [<http://heasarc.gsfc.nasa.gov/docs/xanadu/xspec/index.html>]

Amaud, M. & Raymond, J. 1992, *ApJ*, 398, 394  
 Bennett, C.L., et al. 2003, *ApJS*, 148, 1  
 Bialek, J.J., Evrard, A.E. & Mohr, J.J. 2001, *ApJ*, 555, 597  
 Bialek, J.J., Evrard, A.E. & Mohr, J.J. 2002, *ApJ*, 587, L9  
 Bialek, J.J., Evrard, A.E. & Mohr, J.J. 2005, in preparation

Buote, D A . & Tsai, J C . 1996, *ApJ*, 458, 27

Churazov, E ., Forman, W ., Jones, C ., Sunyaev, R . & B ohringer, H . 2004, *MNRAS*, 347, 29

De Grandi, S ., Ettori, S ., Longhetti & M . Molendi, S . 2004, *A & A*, 419, 7

Dere, et al. 1997, *AA SS*, 125, 149

Dupke, R A . & Amaud, K A . 2001, *ApJ*, 548, 141

Dupke, R A . & Bregman, J N . 2001a, *ApJ*, 547, 705

Dupke, R A . & Bregman, J N . 2001b, *ApJ*, 562, 266

Edge, A C ., Stewart, G C . & Fabian, A C . 1992, *MNRAS*, 258, 177

Evraud, A E . 1988, *MNRAS*, 235, 911

Frenk, C S ., et al. 1999, *ApJ*, 525, 554

Funusho, T ., Mitsuishi, K ., Yamasaki, N ., Fujimoto, R . & Ohashi, T . 2004, *astro-ph/0401490*

Gastaldello, F . & Molendi, S . 2004, *ApJ*, 600, 670

Gil'fanov, M R ., Sunyaev, R A . & Churazov, E M . 1987, *Atom. astron. Zh.* 13, 7

Inogamov, N A . & Sunyaev, R A . 2003, *Astron. Lett.*, 29, 791

Jones, C . & Forman, W . 1984, *ApJ*, 276, 38

Mohr, J J ., Fabricant, D G . & Geller, M J . 1993, *ApJ*, 413, 492

Molendi, S ., M att, G ., Antonelli, L A ., Fiore, F ., Fusco-Femiano, R ., Kaastra, J ., M accarone, C . & Perola, C . 1998, *ApJ* 499, 608

Press, W H ., Teukolsky, S A ., Vetterling, W T . & Flannery, B P . 1992, *Numerical Recipes in Fortran*, 2nd ed., Cambridge University Press

Smith, R K ., Brickhouse, N S ., Liedahl, D A . & Raymond, J C . 2001, *ApJ*, 556, L91 [[http://cxcharvard.edu/atom\\_db//index.htm](http://cxcharvard.edu/atom_db//index.htm)]

Spitzer, L . 1978, *Physical Processes in the Interstellar Medium*, (Wiley, N Y )

Sunyaev, R A ., Norman, M L . & Ryan, G L . 2003, *Astron. Lett.*, 29, 783

Thom as, P A . & Couchman, H M P 1992, *MNRAS*, 257, 11

Ulmer, M P ., C ruddace, R G ., Fritz, G G ., Snyder, W A . & Fenimore, E E . 1987, *ApJ*, 319, 118

Verner, D A ., Verner, E M . & Ferland, G J . 1996, *Atomic Data and Nuclear Tables*, 64, 1

White, R E . III, Day, C S R ., Hatsukade, I . & Hughes, J P . 1994, *ApJ*, 433, 583

Young, et al. 2003, *ApJSS*, 144, 135

This figure "figure1.jpg" is available in "jpg" format from:

<http://arxiv.org/ps/astro-ph/0503281v1>

This figure "figure9.jpg" is available in "jpg" format from:

<http://arxiv.org/ps/astro-ph/0503281v1>

This figure "figure10.jpg" is available in "jpg" format from:

<http://arxiv.org/ps/astro-ph/0503281v1>

This figure "figure11.jpg" is available in "jpg" format from:

<http://arxiv.org/ps/astro-ph/0503281v1>

This figure "figure14.jpg" is available in "jpg" format from:

<http://arxiv.org/ps/astro-ph/0503281v1>

This figure "figure15.jpg" is available in "jpg" format from:

<http://arxiv.org/ps/astro-ph/0503281v1>

This figure "figure16.jpg" is available in "jpg" format from:

<http://arxiv.org/ps/astro-ph/0503281v1>